Journal of Physics: Conference Series

PAPER • **OPEN ACCESS**

Characterization of vortex regeneration mechanism in the self-sustaining process of wall-bounded flows using resolvent analysis

To cite this article: H. Jane Bae and Beverley J. McKeon 2020 *J. Phys.: Conf. Ser.* **1522** 012001

Journal of Physics: Conference Series **1522** (2020) 012001 doi:10.1088/1742-6596/1522/1/012001

Characterization of vortex regeneration mechanism in the self-sustaining process of wall-bounded flows using resolvent analysis

H. Jane Bae & Beverley J. McKeon

Graduate Aerospace Laboratories, California Institute of Technology, Pasadena, CA 91125, USA

E-mail: hjbae@caltech.edu

Abstract. The regeneration mechanism of streamwise vortical structures in the self-sustaining process of wall-bounded turbulence is investigated. Resolvent analysis [1] is used to identify the principal forcing mode which produces the maximum amplification of the response modes in the minimal channel for the buffer [2] and logarithmic layer [3]. The identified mode is then projected out from the nonlinear term of the Navier-Stokes equations at each time step from the direct numerical simulations (DNS) of the corresponding minimal channel. The results show that the removal of the principal forcing mode is able to significantly inhibit turbulence for the buffer and logarithmic layer while removing the subsequent modes instead of the principal one only marginally affects the flow. Analysis of the dyadic interactions in the nonlinear term shows that the contributions toward the principal forcing mode come from a limited number of wavenumber interactions. Using conditional averaging, the flow structures that are responsible for generating the principal forcing mode, and thus the nonlinear interaction to self-sustain turbulence, are identified to be spanwise rolls interacting with meandering streaks.

1. Introduction

The structure of near-wall turbulence has been extensively investigated over the past half-century. In the vicinity of the wall, the flow is found to be highly organized, consisting of streamwise rolls and low- and high-speed streaks [4, 5, 6, 7, 8] that are involved in a quasi-periodic regeneration cycle [9, 10, 11, 12, 13]. However, despite the large effort devoted to the subject, questions still remain in understanding the exact mechanisms by which turbulence self-sustains in wall-bounded turbulent shear flows, and the dynamics in which these structures interact is still uncertain.

Important progress was made in the early 1990s using the "minimal flow unit" approach, which revealed that buffer layer streaks can self-sustain even when motions at larger scales are inhibited and that their existence, therefore, relies on an autonomous process [2]. Hamilton *et al.* [14] utilized a similar approach for Couette flow, where either certain velocity modes were suppressed to remove streak formation or disturbances were added to allow streak breakdown. Jiménez & Pinelli [15] further confirmed that this near-wall process is independent of the flow in the logarithmic and outer regions by showing the survival of the near-wall motions in the absence of outer turbulence. The consensus from these studies, along with many others that followed (e.g. [16, 17]), is that the streaks are significantly amplified by the quasi-streamwise vortices via the

lift-up effect; the amplified streaks subsequently undergo a rapid streamwise meandering motion, reminiscent of streak instability or transient growth, which eventually results in breakdown of the streaks and regeneration of new quasi-streamwise vortices. A similar but more disorganized scenario is hypothesized to occur for the logarithmic layer [3, 18]. Streak formation by streamwise vortices has been extensively documented in the literature (e.g. [19, 7, 20, 21, 22, 23]), and streak breakdown has also received considerable attention (e.g. [24, 25, 14, 26, 27]). Regarding the final component of the self-sustaining cycle, the streamwise vortex regeneration through nonlinear interactions, there is a lack of consensus, and many possible mechanisms have been proposed. Coles [28] and Sreenivasan [29] proposed that the streamwise vortices are generated through the Görtler instability mechanism. A closely related Craik-Leibovich instability [30] has also been considered. Jiménez & Moin [2] proposed the tilting of the vorticity into the streamwise direction as a cause. Nikolaidis *et al.* [31] cite the parametric interaction between the fluctuating streamwise mean flow and the streamwise varying perturbations as the main mechanism. However, vortex regeneration seems to be a complicated process that arises from nonlinear interactions, and the exact mechanism is still elusive.

Resolvent analysis [1, 32], which treats the nonlinear term as a forcing term and identifies the forcing mode associated with the most amplified structures, can be useful in shedding light on the nonlinear mechanism behind streamwise vortex regeneration. The resolvent analysis identifies pairs of response (velocity) and forcing (nonlinear) modes and the corresponding amplification factor from the linearized Navier-Stokes operator and has been successful at identifying the most energetic motions in actual turbulent flows by approximating the nonlinear forcing from the interaction of highly amplified coherent structures. It has been shown that a rank-one approximation captures the characteristics of the most energetic modes of wall-bounded turbulent channels [33]. We postulate that the principal (most amplified) forcing mode then must have the largest impact on the flow and, in particular, the regeneration cycle. We show that the turbulence can be suppressed by removing the nonlinear component corresponding to the principal forcing mode, which supports our hypothesis. We further investigate the flow structures that form the principal forcing mode through nonlinear interactions, shedding light to coherent structures involved in this process.

The paper is organized as follows. We first introduce the method used to identify and remove resolvent forcing modes from the nonlinear term computed from the DNS in §2. We then present the resulting changes in the flow statistics as well as the identification of coherent structures involved in this process in §3. Finally, we summarize our findings in §4.

2. Methods

In the following, we consider a channel flow between two parallel walls. The streamwise, wall-normal and spanwise directions are denoted by x, y, and z, respectively. The flow velocities in the corresponding directions are given by u, v, and w. The streamwise and spanwise directions are considered to be periodic. The flow is characterized by the friction Reynolds number $Re_\tau = \delta u_\tau/\nu$, where δ is the half channel height, u_τ is the friction velocity, and ν is the kinematic viscosity.

2.1. Principal forcing modes

The incompressible Navier-Stokes equations of the velocity fluctuations can be Fourier transformed in homogeneous directions and time and reorganized as

$$-\mathrm{i}\omega\tilde{\boldsymbol{u}} + (\boldsymbol{U}\cdot\hat{\nabla})\tilde{\boldsymbol{u}} + (\tilde{\boldsymbol{u}}\cdot\hat{\nabla})\boldsymbol{U} + \hat{\nabla}\tilde{p} - \frac{1}{Re_\tau}\hat{\Delta}\tilde{\boldsymbol{u}} = \tilde{\boldsymbol{f}}, \quad \hat{\nabla}\cdot\tilde{\boldsymbol{u}} = 0, \tag{1}$$

for each (k_x, k_z, ω), where $(\tilde{\cdot})$ is the Fourier transform in time and space, $\tilde{\boldsymbol{u}}(y; k_x, k_z, \omega) = [\tilde{u}, \tilde{v}, \tilde{w}]^T$ is the velocity fluctuation vector, $\tilde{\boldsymbol{f}}(y; k_x, k_z, \omega) = [\tilde{f}_u, \tilde{f}_v, \tilde{f}_w]^T$ denotes the nonlinear

advection terms, $\boldsymbol{U}(y) = [U, V, W]^T$ is the mean velocity vector averaged over homogeneous directions and time, $\tilde{p}(y; k_x, k_z, \omega)$ is the pressure, $\hat{\nabla} = [\mathrm{i}k_x, \partial_y, \mathrm{i}k_z]^T$, and $\hat{\Delta} = \partial_{yy} - k_x^2 - k_z^2$. Here, the triplet (k_x, k_z, ω) is the temporal frequency and the streamwise and spanwise wavenumbers, respectively. Equivalently, we can express this as

$$\begin{bmatrix} \tilde{\boldsymbol{u}}(y; k_x, k_z, \omega) \\ \tilde{p}(y; k_x, k_z, \omega) \end{bmatrix} = \mathcal{H}(k_x, k_z, \omega) \begin{bmatrix} \tilde{\boldsymbol{f}}(y; k_x, k_z, \omega) \\ 0 \end{bmatrix}. \tag{2}$$

We refer to the linear operator $\mathcal{H}(k_x, k_z, \omega)$ as the resolvent operator. The singular value decomposition of the resolvent operator returns an ordered basis pair $\{\tilde{\boldsymbol{\psi}}_j, \tilde{\boldsymbol{\phi}}_j\}$ along with the associated singular value σ_j ($\sigma_1 \geq \sigma_2 \cdots \geq 0$) which can be used to express the resolvent operator as

$$\begin{bmatrix} \tilde{\boldsymbol{u}}(y; k_x, k_z, \omega) \\ \tilde{p}(y; k_x, k_z, \omega) \end{bmatrix} = \sum_{j=1}^{\infty} \sigma_j(k_x, k_z, \omega) \tilde{\boldsymbol{\psi}}_j(y; k_x, k_z, \omega) \left\langle \tilde{\boldsymbol{\phi}}_j(y; k_x, k_z, \omega), \begin{bmatrix} \tilde{\boldsymbol{f}}(y; k_x, k_z, \omega) \\ 0 \end{bmatrix} \right\rangle, \tag{3}$$

where $\langle \cdot, \cdot \rangle$ is the inner product corresponding to the kinetic energy norm, and the basis $\tilde{\boldsymbol{\phi}}_i$ and $\tilde{\boldsymbol{\psi}}_i$ are unitary. We refer to $\tilde{\boldsymbol{\psi}}_j$ as the response modes and $\tilde{\boldsymbol{\phi}}_j$ as the forcing modes. The former identifies the most amplified coherent structures, which are considered to contain most of the energy. The latter are the basis for the nonlinear terms that create the response modes via the linear resolvent operator.

Note that due to the symmetry in the channel flow, the resolvent modes occur in pairs with the same singular value. While any linear combination of the two resolvent modes corresponding to the largest singular value σ_1 can be considered the principal mode, we focus on the principal forcing mode $\tilde{\boldsymbol{\phi}}_1 = [\tilde{\phi}_{1,u}, \tilde{\phi}_{1,v}, \tilde{\phi}_{1,w}, 0]^T$ with the support isolated to one half (bottom) of the channel such that the projection of the resolvent mode will only be directly affected by flow in the bottom half of the channel.

2.2. Numerical simulation

The simulations are performed by discretizing the incompressible Navier-Stokes equations with a staggered, second-order accurate, central finite-difference method in space [34], and an explicit third-order accurate Runge-Kutta method for time advancement [35]. The system of equations is solved via an operator splitting approach [36]. Periodic boundary conditions are imposed in the streamwise and spanwise directions, and the no-slip condition is applied at the walls. The code has been validated in previous studies of turbulent channel flows [37, 38, 39]. The resolvent modes were computed using the same staggered, second-order accurate, central finite difference method in the wall-normal direction. The Fourier discretization in the computation of the resolvent modes in the streamwise and spanwise directions was modified to use the modified wavenumber corresponding to a staggered second-order finite-difference method.

We perform two sets of DNS of incompressible turbulent channel flow to investigate the self-sustaining process at different scales, where each simulation is performed within a computational domain tailored to isolate the dynamics in either the buffer or the logarithmic layer. For the buffer layer case with $Re_\tau \approx 186$ (CH180B), the streamwise, wall-normal, and spanwise domain sizes are $L_x^+ \approx 340$, $L_y^+ \approx 372$ and $L_z^+ \approx 170$, respectively. Jiménez & Moin [2] showed that simulations in this domain constitute an elemental structural unit containing a single streamwise streak and a pair of staggered quasi-streamwise vortices, which reproduce reasonably well the statistics of the flow in larger domains. The case at $Re_\tau \approx 930$ (CH950L) was computed for the minimal unit for the logarithmic layer with $L_x^+ \approx 1450$, $L_y^+ \approx 1860$ and $L_z^+ \approx 726$, respectively. These dimensions correspond to a minimal box simulation for the logarithmic layer and are considered to be sufficient to isolate the relevant dynamical structures involved in the bursting

Table 1: Tabulated list of cases. The CH180B case corresponds to the minimal box for the simulations of the buffer layer and the CH950L case corresponds to the minimal box for the simulations of the logarithmic layer. CH950B is the buffer layer simulation for the taller domain.

Case	Re_τ	L_x^+	L_z^+	L_y^+	Δ_x^+	Δ_z^+	$\min(\Delta_y^+)$	$\max(\Delta_y^+)$
CH180B	186	340	170	372	10.6	5.3	0.17	7.6
CH950L	930	1450	726	1860	7.6	3.8	0.28	12.7
CH950B	930	340	170	1860	7.6	3.8	0.28	12.7

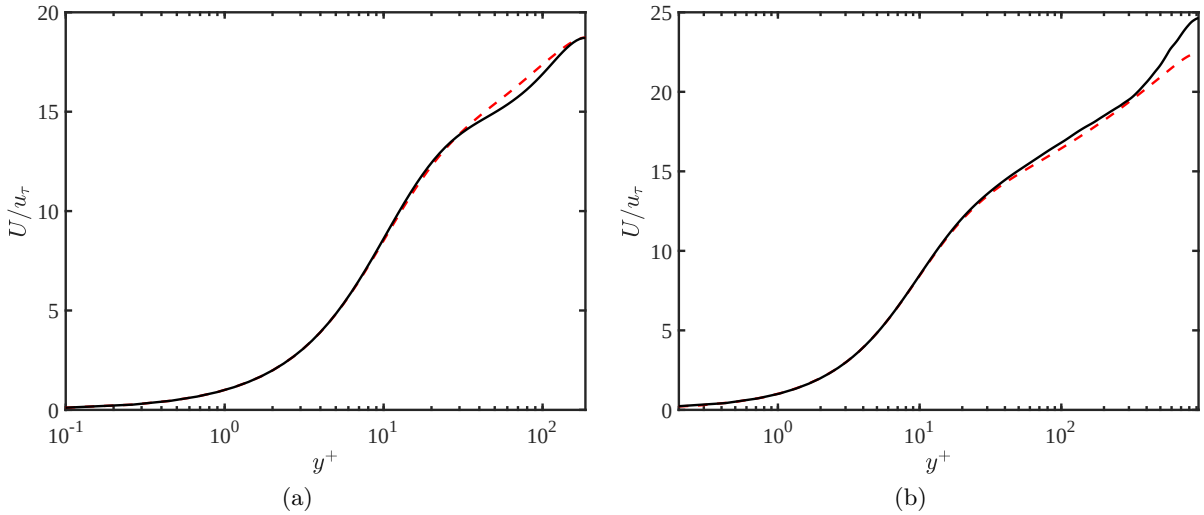

Figure 1: Mean streamwise velocity profile of the (a) buffer layer minimal channel at $Re_\tau \approx 186$ and (b) the log layer minimal channel at $Re_\tau \approx 930$ (——), compared to the mean velocity profile of the channel flow for the domain size of $12\pi\delta \times 2\delta \times 4\pi$ or $8\pi\delta \times 2\delta \times 4\pi$, respectively, (– – –) at corresponding friction Reynolds numbers [40].

process [3]. An additional case with $L_x^+ \approx 340$, $L_y^+ \approx 1860$ and $L_z^+ \approx 170$ (CH950B) was performed to isolate the buffer layer dynamics that are independent of the logarithmic layer dynamics in the $Re_\tau \approx 930$ case [15], which is later used to compare against the CH950L case. The grid spacings in the streamwise and spanwise directions are uniform; non-uniform meshes are used in the wall-normal direction, with the grid stretched toward the wall according to a hyperbolic tangent distribution. The details of the simulation and the grid resolutions for each case are summarized in Table 1.

The flow is simulated for more than $50\delta/u_\tau$ after transients for computation of the mean streamwise velocity profile, $U(y)$, shown in Figure 1. Once the mean velocity profile has converged, a separate simulation with the mean $U(y)$ frozen in time by an appropriate forcing at each time step is performed. The mean velocity profile is frozen so that the most amplified resolvent modes remain constant throughout the simulation. It also aligns with the aim of the study, which is to characterize the mechanisms that sustain the turbulent mean state. Once a statistically steady state is reached, the simulation is advanced in time by removing the

projection of the Fourier transformed (in homogeneous directions only) nonlinear term, $\hat{\boldsymbol{f}}$, onto $\tilde{\boldsymbol{\phi}}_1$, *i.e.*,

$$\hat{\boldsymbol{g}}_1(y;k_x,k_z) = \left\langle \begin{bmatrix} \hat{\boldsymbol{f}}(y,k_x,k_z) \\ 0 \end{bmatrix}, \tilde{\boldsymbol{\phi}}_1(y;k_x,k_z,\omega) \right\rangle \begin{bmatrix} \tilde{\boldsymbol{\phi}}_{1,u}(y;k_x,k_z,\omega) \\ \tilde{\boldsymbol{\phi}}_{1,v}(y;k_x,k_z,\omega) \\ \tilde{\boldsymbol{\phi}}_{1,w}(y;k_x,k_z,\omega) \end{bmatrix}, \tag{4}$$

from $\hat{\boldsymbol{f}}$ for a given (k_x,k_z,ω) at each time step. Projections onto $\tilde{\boldsymbol{\phi}}_i$ are analogously defined as $\hat{\boldsymbol{g}}_i$. Symmetry of the Fourier modes is preserved by also removing $\hat{\boldsymbol{g}}_1^*$, the conjugate of $\hat{\boldsymbol{g}}_1$, from the nonlinear term $\hat{\boldsymbol{f}}(y;-k_x,-k_z)$ at each time step. This projection includes the contributions from various temporal frequencies apart from the specified ω. However, it ascertains the removal of this particular forcing mode. Later, in §2.3, we show that our particular choice of ω is such that the singular value associated with the chosen ω is much larger than other temporal frequencies, making the removal of other frequency contents relatively less significant.

For the remainder of the paper, we denote the channel flow simulation with the mean fixed at each time step but no forcing mode removed as the *undamped* case and the simulation with the forcing mode removed as the *damped* case.

2.3. Choice of target wavenumbers

As mentioned in the previous section, a choice of the target wavenumbers is required to identify the forcing modes that are removed at each time step. For this, we target the Fourier modes with the most energy content. Figure 2(a) shows the spectral energy content, $\hat{E}(y,k_x,k_z) = 1/2\,(\hat{\boldsymbol{u}}^*\hat{\boldsymbol{u}})$, in the buffer layer ($y^+ \approx 15$) of the minimal channel CH180B as a function of streamwise and spanwise wavenumber. There is a clear peak at $(k_xL_x/2\pi, k_zL_z/2\pi) = (0,\pm1)$. This is consistent with the fact that the domain size of the minimal channel is such that it isolates flow structures to be infinitely long in the streamwise direction and once-periodic in the spanwise direction. Thus, for our analysis, we choose the streamwise and spanwise wavenumbers $(k_xL_x/2\pi, k_zL_z/2\pi) = (0,1)$. The temporal frequency is given as $\omega = 0$ since the $k_xL_x/2\pi = 0$ wavenumber identifies the streamwise stationary mode, and the convective velocity of this mode is zero. While not shown, the case CH950L also shows similar spectral energy content in the logarithmic layer ($y/\delta \approx 0.2$), and thus the same set of wavenumbers are chosen for the analysis. As mentioned in §2.2, we do remove other frequency content by removing the projection of $\tilde{\boldsymbol{\phi}}_1$. However, first of all, the principal forcing mode of $\omega = 0$ is not identical to that of other frequencies, and removing $\tilde{\boldsymbol{\phi}}_1$ for $(k_xL_x/2\pi, k_zL_z/2\pi, \omega) = (0,1,0)$ does not completely remove the principal forcing modes for other temporal frequencies. Moreover, the singular values as a function of ω (Figure 2(b)) show that the most amplified structure of the given (k_x,k_z) pair is given by $\omega = 0$.

The principal forcing modes of CH180B and CH950L for this particular frequency-wavenumber triplet are given in Figure 2(c) and 2(d), respectively. In both cases, the forcing mode highlights a pair of streamwise rolls spanning the entire channel half-height. A much weaker streamwise streak whose magnitude ($|\tilde{\boldsymbol{\phi}}_{1,u}|$) is approximately 5% (CH180B) or 1% (CH950L) of that of the streamwise rolls, $(\tilde{\boldsymbol{\phi}}_{1,v}^2 + \tilde{\boldsymbol{\phi}}_{1,w}^2)^{1/2}$, is also present. The values above $y/\delta = 1$ are negligible due to our definition of the principal forcing mode. For the given (k_x,k_z,ω), the principal forcing mode contains the largest energetic contribution (approximately 85%), defined as $\sigma_i^2/\sum_{k=1}^{\infty}\sigma_k^2$ for each $\tilde{\boldsymbol{\phi}}_i$. The subsequent modes $\tilde{\boldsymbol{\phi}}_2$ and $\tilde{\boldsymbol{\phi}}_3$ have an energetic contribution of approximately 12% and 2%, respectively. The large separation in the singular values indicates that the principal forcing mode will be amplified by almost an order of magnitude more than the other forcing modes and thus will be integral in the self-sustaining process.

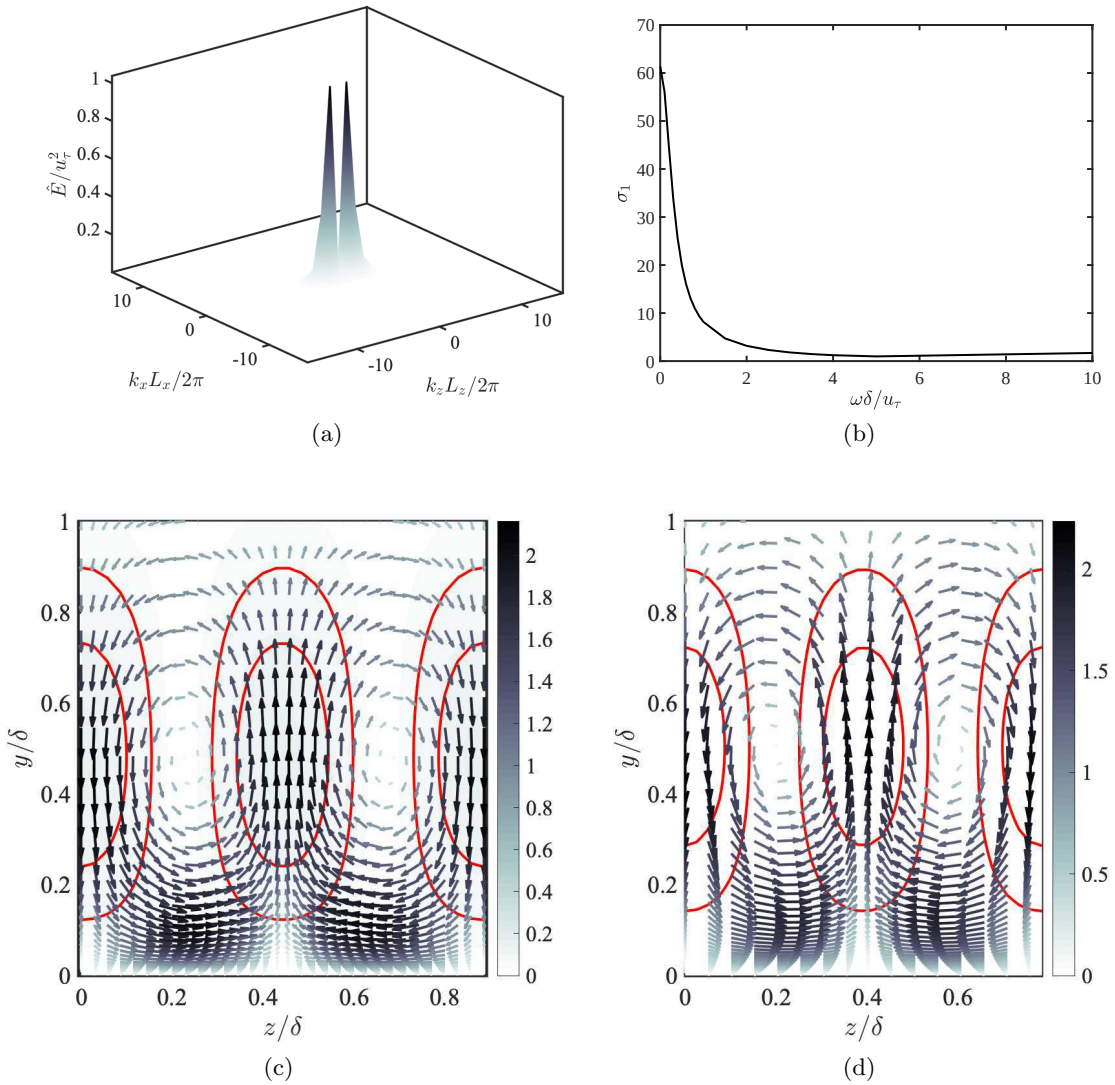

Figure 2: (a) Spectral energy content, $\hat{E}$, at $y^+ \approx 15$ for the minimal channel at $Re_\tau \approx 186$. (b) Principal singular value σ_1 as a function of ω for $(k_xL_x/2\pi, k_zL_z/2\pi) = (0, 1)$. (c) The y-z plane of the principal forcing mode $\tilde{\phi}_1$ for $(k_xL_x/2\pi, k_zL_z/2\pi, \omega) = (0, 1, 0)$ for CH180B. The streamwise component $|\tilde{\phi}_{1,u}|$ (color) and the cross-flow component $(\tilde{\phi}_{1,v}^2 + \tilde{\phi}_{1,w}^2)^{1/2}$ (quiver) are given, with the color bar indicating magnitude for both components. The contour lines (——) indicate streamwise magnitudes that are 3% and 5% of the maximum cross-flow magnitudes. (d) Same as (c) but for CH950L. The contour lines (——) indicate streamwise magnitudes that are 0.5% and 0.9% of the maximum cross-flow magnitudes.

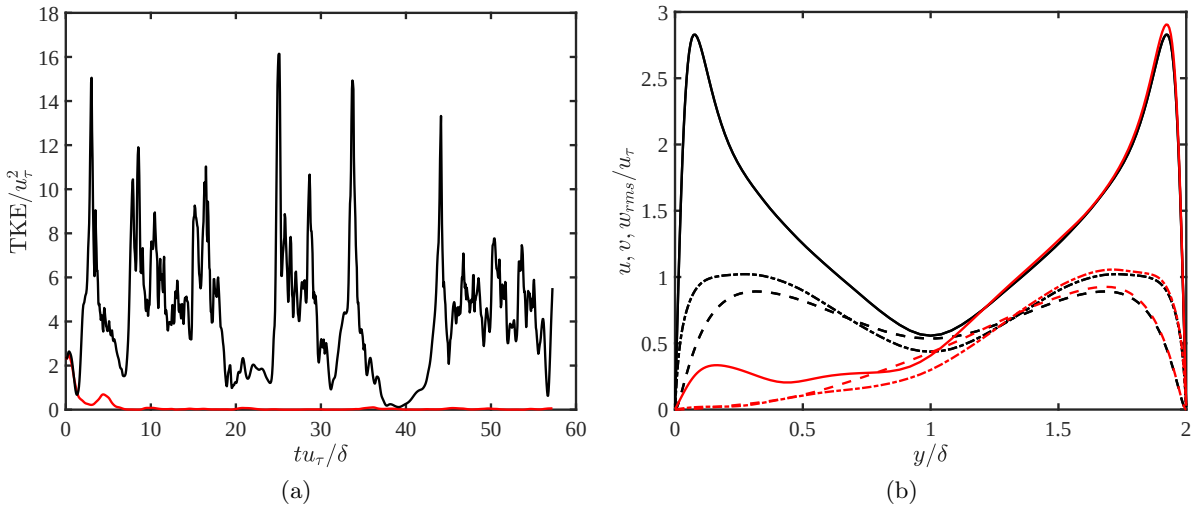

Figure 3: (a) Temporal evolution of TKE at $y^+ \approx 15$ for the undamped minimal channel (——) and the undamped minimal channel (——) at $Re_\tau \approx 186$. (b) Streamwise (——), wall-normal (– – –), and spanwise (— · —) rms velocity fluctuations for the damped (red) and the undamped (black) minimal channel.

3. Results

3.1. Time evolution of turbulence kinetic energy and turbulence intensities

The effect of removing $\hat{\boldsymbol{g}}_1$ for the case CH180B can be seen in Figure 3(a) in the form of the turbulence kinetic energy (TKE) evolution in time. It shows that removing $\hat{\boldsymbol{g}}_1$ reduces the TKE significantly. The steady-state root-mean-square (rms) velocity fluctuation profiles for this case are given in Figure 3(b). As expected, the effect of removing the principal forcing term is observed only on the bottom half of the channel where the principal forcing term was isolated, with only minor changes in the statistics in the top half of the channel. At any instance of time of the undamped case, the average contribution of $\hat{\boldsymbol{g}}_1$ to the total advection term is less than 0.9%, and removing the same magnitude randomly from the advection term at each time step had no effect on the first-order statistics. Thus, the spatial structure of the mode that is being projected out is essential in the laminarization of the flow.

We also repeat the previous experiment, but removing either $\hat{\boldsymbol{g}}_2$ or $\hat{\boldsymbol{g}}_3$ instead of $\hat{\boldsymbol{g}}_1$ in the CH180B. We see that turbulence is sustained in both cases from Figure 4(a), but the extreme peaks in TKE observed in the undamped case are not as prominent. We can also see in Figure 4(b) that while the effect of removing $\hat{\boldsymbol{g}}_2$ still has some impact on the steady-state turbulence intensities, especially around $y^+ \approx 15$, the net change in the statistics is much smaller than that of removing $\hat{\boldsymbol{g}}_1$. Removing $\hat{\boldsymbol{g}}_3$ has no impact on first-order statistics, and similar results are expected of subsequent forcing modes. At any instance of time, the average contribution of $\hat{\boldsymbol{g}}_2$ or $\hat{\boldsymbol{g}}_3$ in the undamped case are statistically similar to the contribution of $\hat{\boldsymbol{g}}_1$ at 0.9% of the total advection term, which supports the impact of the principal forcing mode on the turbulent flow. This demonstrates the capability of resolvent analysis in identifying important fluid structures.

In the case of CH950L, as shown in Figure 5(a), the TKE does not vanish but is small compared to the undamped case such that the average TKE for the damped case is comparable to the minimum value of TKE for the undamped case. The steady-state rms fluctuating velocities (Figure 5(b)) show a clear decrease in the logarithmic region of the bottom half of the channel.

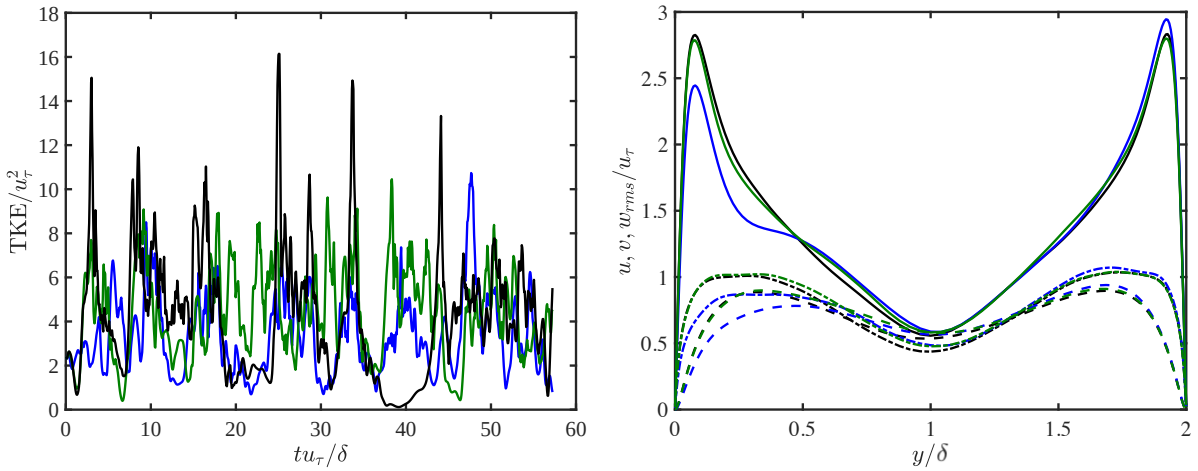

Figure 4: (a) Temporal evolution of TKE at $y^+ \approx 15$ for the minimal channel at $Re_\tau \approx 186$ removing $\hat{\boldsymbol{g}}_2$ (——) or $\hat{\boldsymbol{g}}_3$ (——) at each time step. The TKE for the undamped minimal channel is given for comparison (——). (b) Streamwise (——), wall-normal (– – –), and spanwise (— · —) rms velocity fluctuations of damping $\hat{\boldsymbol{g}}_2$ at each time step (blue), $\hat{\boldsymbol{g}}_3$ at each time step (green), and the undamped minimal channel (black).

The remaining turbulence intensities can be attributed to the transport of energy from the buffer layer dynamics, which are still sustained as the resolvent mode is centered around the logarithmic region and has no impact on the inner region. The larger box for the logarithmic layer isolates more complicated, fully multiscale structures that reach from the wall farther into the core flow, making it harder to isolate individual flow features to be studied as in the buffer layer case. A separate undamped DNS (CH950B) is performed to demonstrate the turbulence intensities due to buffer layer dynamics. The results in Figure 5(b) show that the damped CH950L case exhibit lower levels of turbulence in the logarithmic region even compared to the undamped CH950B case, showing that the removal of the principal forcing mode effectively removes the logarithmic layer contributions to the turbulence intensities and the remaining turbulence is generated by the energy transfer from the buffer layer.

3.2. Nonlinear interaction

As demonstrated above, the principal forcing mode $\tilde{\boldsymbol{\phi}}_1$ identifies the most amplified nonlinear interaction and is integral in sustaining turbulence in the near wall cycle. In order to study the nonlinear interactions that produce this term through dyadic interactions, we decompose the nonlinear term as a convolution sum in Fourier space

$$\hat{\boldsymbol{f}}(y;k_x,k_z) = \sum_{k_x',k_z'=-\infty}^{\infty} \left(\hat{\boldsymbol{u}}(y;k_x',k_z')\cdot\hat{\nabla}\right)\hat{\boldsymbol{u}}(y;k_x-k_x',k_z-k_z'), \tag{5}$$

where $\hat{\nabla} = [\mathrm{i}k_x, \partial_y, \mathrm{i}k_z]^T$. The contribution of each component of the convolution sum toward the projection of the principal forcing term for any given flow field can be measured as

$$\Pi(k_x',k_z';k_x,k_z) = \left\langle \begin{bmatrix} \left(\hat{\boldsymbol{u}}(y;k_x',k_z')\cdot\hat{\nabla}\right)\hat{\boldsymbol{u}}(y;k_x-k_x',k_z-k_z') \\ 0 \end{bmatrix}, \tilde{\boldsymbol{\phi}}_1(y;k_x,k_z,\omega) \right\rangle, \tag{6}$$

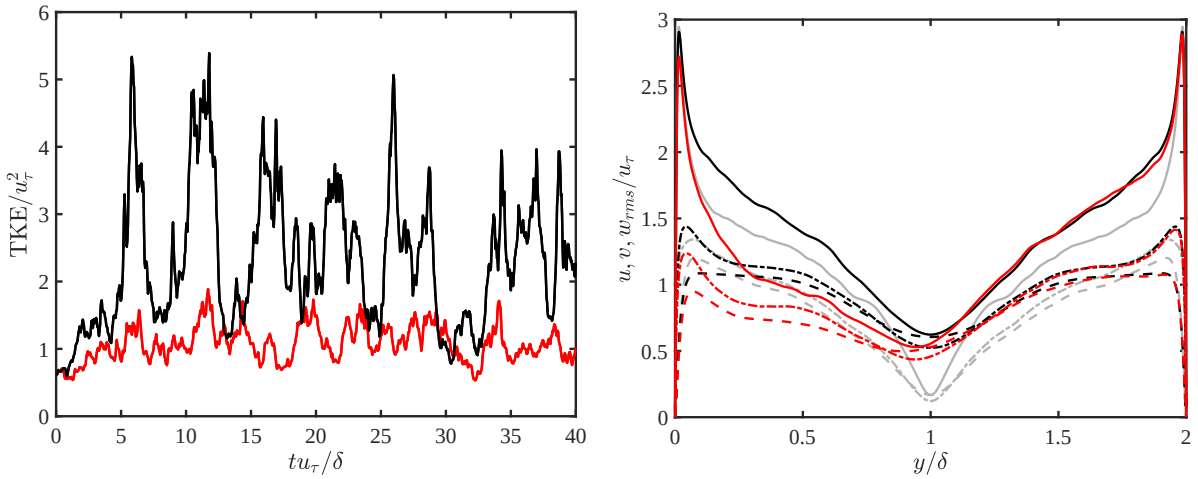

Figure 5: (a) Temporal evolution of TKE at $y/h \approx 0.35$ for the damped minimal channel (——) and the undamped minimal channel (——) at $Re_\tau \approx 930$. (b) Streamwise (——), wall-normal (– – –), and spanwise (— · —) rms velocity fluctuations of the damped channel (red) and the undamped minimal channel (black) at $Re_\tau \approx 930$. The rms velocity fluctuations for the minimal channel of the buffer layer at $Re_\tau \approx 930$ (gray) is also shown for comparison.

where $(k_x L_x/2\pi, k_z L_z/2\pi) = (0, 1)$ as before. Note that integration over all k_x' and k_z' of $\Pi(k_x', k_z'; k_x, k_z)$ gives the projection coefficient computed in Eq. (4). Also, due to incompressibility, Π is symmetric with respect to (k_x, k_z) for each flow field; that is, $\Pi(k_x', k_z'; k_x, k_z) = \Pi(k_x - k_x', k_z - k_z'; k_x, k_z)$. The average spectral map of $|\Pi(k_x', k_z'; k_x, k_z)|$ normalized by the total contribution $|\sum_{k_x', k_z'} \Pi(k_x', k_z'; k_x, k_z)|$ is computed from flow fields of the undamped minimal channel at $Re_\tau \approx 186$ for $k_x L_x/2\pi = 0$ and $k_z L_z/2\pi = 1$ and is depicted in Figure 6. The spectral map identifies two main sources of contribution from the wavenumber pair $(k_x' L_x/2\pi, k_z' L_z/2\pi) = (\pm 1, 0)$ (and from symmetry $(k_x' L_x/2\pi, k_z' L_z/2\pi) = (\mp 1, 1)$), which account for approximately 40% of the total contribution. While the contributions from other wavenumber pairs are not negligible, for the remainder of this paper, we focus on these two sets of wavenumbers to identify the coherent structures responsible for the nonlinear forcing term. In particular, since the two sets are mere mirror images in the x-plane, we focus on only one of the two cases, namely $(k_x' L_x/2\pi, k_z' L_z/2\pi) = (1, 0)$ with $((k_x - k_x') L_x/2\pi, k_z - k_z' L_z/2\pi) = (-1, 1)$.

To identify instantaneous flow configurations where the contribution towards $\tilde{\boldsymbol{\phi}}_1$ is strong or weak, we first observe values of $\bar{\Pi}(k_x', k_z') = |\Pi(k_x', k_z')| / \langle \hat{\boldsymbol{f}}(k_x', k_z'), \hat{\boldsymbol{f}}(k_x', k_z') \rangle^{1/2}$, which represents the normalized contribution to the principal forcing term with respect to the total energy of the nonlinear term in the (k_x', k_z') mode, computed from flow fields of the undamped channel. We then determine the mean μ and standard deviation ς of the distribution of $\bar{\Pi}(k_x', k_z')$ over all time instances. The high forcing-intensity events are defined as those with $\bar{\Pi}(k_x', k_z') > \mu + 2\varsigma$ and low forcing-intensity events as those with $\bar{\Pi}(k_x', k_z') < \mu - 2\varsigma$. Both cases consist of approximately 5% of the total events. Note that for events in both categories, the total energy in the (k_x', k_z') mode, $\langle \hat{\boldsymbol{f}}(k_x', k_z'), \hat{\boldsymbol{f}}(k_x', k_z') \rangle$, was similarly distributed.

The average $\mathcal{F}^{-1}\hat{\boldsymbol{u}}(k_x', k_z')$ and $\mathcal{F}^{-1}\hat{\boldsymbol{u}}(k_x - k_x', k_z - k_z')$ conditioned to high forcing-intensity events are shown in Figure 7, where $\mathcal{F}^{-1}$ is the inverse Fourier transform. The modes are phase shifted before averaging such that they are phase aligned for the streamwise velocity component at $y^+ \approx 40$. The coherent structures identified by the (k_x', k_z') mode are in the form of a

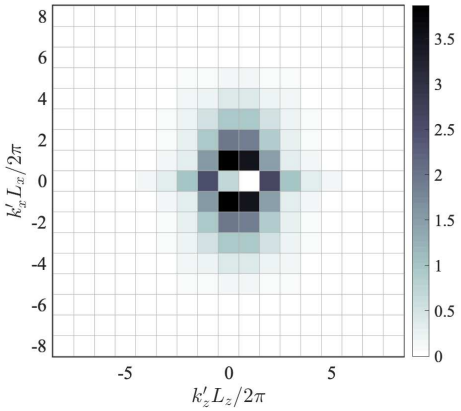

Figure 6: Average contribution of each convolution sum $|\Pi(k'_x, k'_z)|$ normalized by the total contribution $\left|\sum_{k'_x,k'_z} \Pi(k'_x, k'_z)\right|$ for $k_x L_x/2\pi = 0$ and $k_z L_z/2\pi = 1$ for channel flow at $Re_\tau \approx 186$.

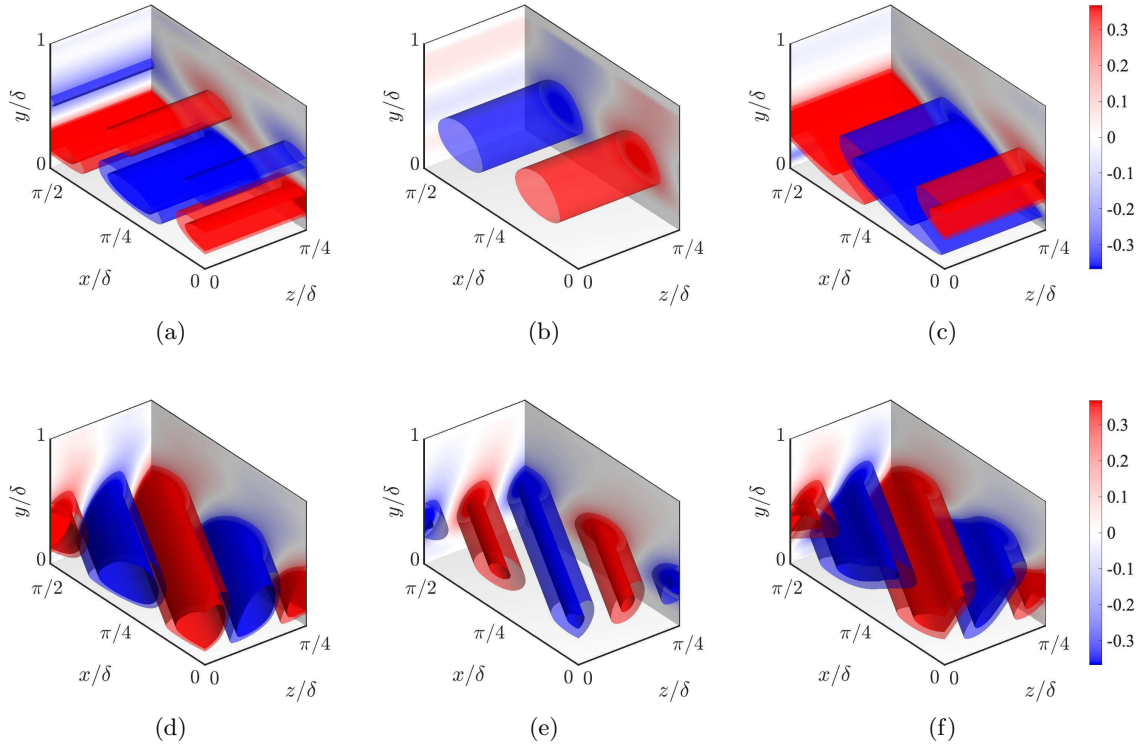

Figure 7: Average (a) $\mathcal{F}^{-1}\hat{u}$, (b) $\mathcal{F}^{-1}\hat{v}$, (c) $\mathcal{F}^{-1}\hat{w}$ for (k'_x, k'_z) and (d) $\mathcal{F}^{-1}\hat{u}$, (e)$\mathcal{F}^{-1}\hat{v}$, (f) $\mathcal{F}^{-1}\hat{w}$ for $(k_x - k'_x, k_z - k'_z)$ conditioned to high forcing-intensity events shown in physical coordinates for $Re_\tau \approx 186$. The surface plots are in wall units with values indicated by the colorbar. The isosurfaces are values corresponding to 0.41 (solid red), 0.26 (transparent red), -0.26 (transparent blue), and -0.41 (solid blue).

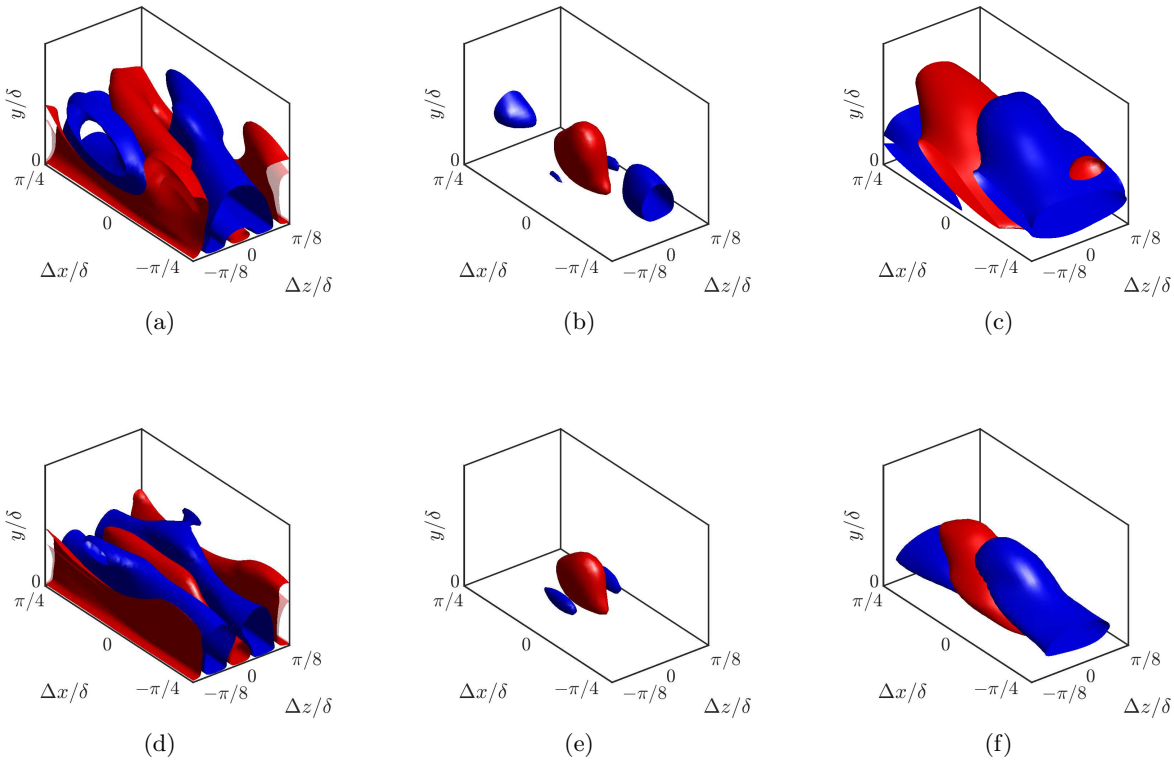

Figure 8: Correlations (a,d) C_{uu}, (b,e) C_{vv}, and (c,f) C_{ww} conditioned to (a,b,c) high forcing-intensity and (d,e,f) low forcing-intensity events for $Re_\tau \approx 186$. The isosurfaces are 0.1 (red) and -0.04 (blue).

pair of spanwise rolls that is being sheared in the spanwise direction. The $(k_x - k'_x, k_z - k'_z)$ mode show meandering streaks, with high-speed streaks moving towards the wall and low-speed streaks moving away from the wall, corresponding to sweeps and ejections. Furthermore, the spatial auto-correlation coefficients of the streamwise, wall-normal, and spanwise velocity fluctuations, denoted C_{uu}, C_{vv}, and C_{ww} respectively, are computed conditioned to high forcing-intensity events at the same wall-normal location $y^+ \approx 40$. The correlations shown in Figure 8(a,b,c) reveal structures very similar to ones highlighted by the time-averaged $\mathcal{F}^{-1}\hat{\boldsymbol{u}}(k'_x, k'_z)$ and $\mathcal{F}^{-1}\hat{\boldsymbol{u}}(k_x - k'_x, k_z - k'_z)$ and resemble spanwise-sheared spanwise rolls (C_{vv} and C_{ww}) with meandering streaks (C_{uu}).

On the contrary, although not shown, $\mathcal{F}^{-1}\hat{\boldsymbol{u}}(k'_x, k'_z)$ and $\mathcal{F}^{-1}\hat{\boldsymbol{u}}(k_x - k'_x, k_z - k'_z)$ conditioned to low forcing-intensity events are less coherent for these wave parameters and show no visible structures using the same threshold as Figure 7. This can be observed from the conditional correlation in Figure 8(d,e,f), where the streamwise and wall-normal velocities only show structures resembling straight streaks and no structures resembling meandering streaks or spanwise rolls as in Figure 8(a,b,c). The spanwise shear component C_{ww} shown in Figure 8(f) also has a much narrower footprint in the spanwise direction compared to its counterpart in Figure 8(c). Considering the fact that the total kinetic energy distribution for the strong and weak events are similar, these results show that the precursor to the nonlinear interaction that generates the principal forcing mode has more defined coherent structures in the form of

spanwise rolls and meandering streaks, which interact to produce the principal forcing mode, which then plays an important role in the self-sustaining cycle of near-wall turbulence.

4. Conclusions

We have studied the self-sustaining process of wall-bounded turbulence with special emphasis on mechanisms involved in regenerating streamwise vortices. Vortex regeneration seems to be a complicated process that arises from nonlinear interactions, and the exact underlying mechanism is still elusive. For this purpose, we have utilized resolvent analysis to identify the most amplified nonlinear term in the incompressible Navier-Stokes equations and studied the effect of this term on DNS of turbulent channel flow.

Simulations of the minimal channel for the buffer and logarithmic layer with a fixed mean streamwise velocity profile were performed to isolate the structures at a prescribed scale. The most amplified nonlinear term corresponding to the most energetic wavenumber was then computed from the resolvent analysis using the mean velocity profile of the minimal channel simulations. The identified mode was removed from the nonlinear term of a DNS for a minimal channel simulation with a fixed mean velocity profile at each time step. We have shown that the removal of the principal forcing mode leads to a significant decrease in turbulence intensities, with the flow laminarizing in the buffer layer case. In the logarithmic layer case, the non-laminarization was attributed to the turbulence generated in the buffer-layer that survives regardless of the logarithmic layer dynamics. We also applied the removal method for subsequent forcing modes instead, and observed an only marginal decrease in the turbulence intensities, which reinstates the principal forcing mode as the most amplified, and thus the most important, component of the nonlinear term.

In addition, we identified the coherent structures that, through the nonlinear interaction, form the principal forcing mode. The identified structures are in the form of spanwise-sheared spanwise rolls and meandering streaks. The interaction of these two coherent structures is similar to the tilting of the vorticity into the streamwise direction, which was a phenomenon proposed by Jiménez & Moin [2] as the mechanisms of vortex regeneration. The interaction of the two components highlighted here regenerates streamwise vortices, which through the lift-up mechanism amplifies streamwise streaks. These streamwise streaks break down from instability, which spawn new generations of meandering streaks and spanwise rolls, completing the self-sustaining process.

Acknowledgments

This work was funded in part by the Coturb program of the European Research Council. The authors thank Dr. Adrián Lozano-Durán, Dr. Yongseok Kwon, and Dr. Anna Guseva for their insightful comments.

References

[1] B. J. McKeon and A. S. Sharma. A critical-layer framework for turbulent pipe flow. *J. Fluid Mech.*, 658:336–382, 2010.

[2] J. Jiménez and P. Moin. The minimal flow unit in near-wall turbulence. *J. Fluid Mech.*, 225:213–240, 4 1991.

[3] O. Flores and J. Jiménez. Hierarchy of minimal flow units in the logarithmic layer. *Phys. Fluids*, 22(7):071704, 2010.

[4] P. S. Klebanoff, K. D. Tidstrom, and L. M. Sargent. The three-dimensional nature of boundary-layer instability. *J. Fluid Mech.*, 12(1):1–34, 1962.

[5] S. J. Kline, W. C. Reynolds, F. A. Schraub, and P. W. Runstadler. The structure of turbulent boundary layers. *J. Fluid Mech.*, 30(4):741–773, 1967.

[6] C. R. Smith and S. P. Metzler. The characteristics of low-speed streaks in the near-wall region of a turbulent boundary layer. *J. Fluid Mech.*, 129:27–54, 1983.

[7] R. F. Blackwelder and H. Eckelmann. Streamwise vortices associated with the bursting phenomenon. *J. Fluid Mech.*, 94(3):577–594, 1979.

[8] A. V. Johansson, J.-Y. Her, and J. H. Haritonidis. On the generation of high-amplitude wall-pressure peaks in turbulent boundary layers and spots. *J. Fluid Mech.*, 175:119–142, 1987.

[9] S. K. Robinson. Coherent motions in the turbulent boundary layer. *Ann. Rev. Fluid Mech.*, 23(1):601–639, 1991.

[10] R. L. Panton. Overview of the self-sustaining mechanisms of wall turbulence. *Prog. Aerosp. Sci.*, 37(4):341–383, 2001.

[11] R. J. Adrian. Hairpin vortex organization in wall turbulence. *Phys. Fluids*, 19(4):041301, 2007.

[12] A. J. Smits, B. J. McKeon, and I. Marusic. High–Reynolds number wall turbulence. *Ann. Rev. Fluid Mech.*, 43, 2011.

[13] J. Jiménez. Coherent structures in wall-bounded turbulence. *J. Fluid Mech.*, 842, 2018.

[14] J. M. Hamilton, J. Kim, and F. Waleffe. Regeneration mechanisms of near-wall turbulence structures. *J. Fluid Mech.*, 287:317–348, 1995.

[15] J. Jiménez and A. Pinelli. The autonomous cycle of near-wall turbulence. *J. Fluid Mech.*, 389:335–359, 1999.

[16] F. Waleffe. On a self-sustaining process in shear flows. *Phys. Fluids*, 9(4):883–900, 1997.

[17] B. F. Farrell, D. F. Gayme, and P. J. Ioannou. A statistical state dynamics approach to wall turbulence. *Philos. Trans. Royal Soc.*, 375(2089):20160081, 2017.

[18] C. Cossu and Y. Hwang. Self-sustaining processes at all scales in wall-bounded turbulent shear flows. *Philos. Trans. Royal Soc.*, 375(2089):20160088, 2017.

[19] H. P. Bakewell Jr and J. L. Lumley. Viscous sublayer and adjacent wall region in turbulent pipe flow. *Phys. Fluids*, 10(9):1880–1889, 1967.

[20] M. T. Landahl. A note on an algebraic instability of inviscid parallel shear flows. *J. Fluid Mech.*, 98(2):243–251, 1980.

[21] K. M. Butler and B. F. Farrell. Optimal perturbations and streak spacing in wall-bounded turbulent shear flow. *Phys. Fluids A*, 5(3):774–777, 1993.

[22] S. I. Chernyshenko and M. F. Baig. The mechanism of streak formation in near-wall turbulence. *J. Fluid Mech.*, 544:99–131, 2005.

[23] J. C. Del Alamo and J. Jiménez. Linear energy amplification in turbulent channels. *J. Fluid Mech.*, 559:205–213, 2006.

[24] H. T. Kim, S. J. Kline, and W. C. Reynolds. The production of turbulence near a smooth wall in a turbulent boundary layer. *J. Fluid Mech.*, 50(1):133–160, 1971.

[25] J. D. Swearingen and R. F. Blackwelder. The growth and breakdown of streamwise vortices in the presence of a wall. *J. Fluid Mech.*, 182:255–290, 1987.

[26] F. Waleffe. Transition in shear flows. nonlinear normality versus non-normal linearity. *Phys. Fluids*, 7(12):3060–3066, 1995.

[27] W. Schoppa and F. Hussain. Coherent structure generation in near-wall turbulence. *J. Fluid Mech.*, 453:57–108, 2002.

[28] D. Coles. A model for flow in the viscous sublayer. In *Workshop on coherent structure of turbulent boundary layers*, pages 462–475, 1978.

[29] K. R. Sreenivasan. A unified view of the origin and morphology of the turbulent boundary layer structure. In *Turbulence Management and Relaminarisation*, pages 37–61. Springer, 1988.

[30] A. D. D. Craik and S. Leibovich. A rational model for langmuir circulations. *J. Fluid Mech.*, 73(3):401–426, 1976.

[31] M.-A. Nikolaidis, B. F. Farrell, and P. J. Ioannou. The mechanism by which nonlinearity sustains turbulence in plane couette flow. In *J. Phys. Conf. Ser.*, volume 1001, page 012014. IOP Publishing, 2018.

[32] B. J. McKeon. The engine behind (wall) turbulence: perspectives on scale interactions. *J. Fluid Mech.*, 817, 2017.

[33] R. Moarref, A. S. Sharma, J. A. Tropp, and B. J. McKeon. Model-based scaling of the streamwise energy density in high-Reynolds-number turbulent channels. *J. Fluid Mech.*, 734:275–316, 2013.

[34] P. Orlandi. *Fluid Flow Phenomena: A Numerical Toolkit.* Fluid Flow Phenomena: A Numerical Toolkit. Springer, 2000.

[35] A. A. Wray. Minimal-storage time advancement schemes for spectral methods. Technical report, NASA Ames Research Center, 1990.

[36] A. J. Chorin. Numerical solution of the Navier-Stokes equations. *Math. Comput.*, 22(104):745–762, 1968.

[37] A. Lozano-Durán and H. J. Bae. Turbulent channel with slip boundaries as a benchmark for subgrid-scale models in LES. *Center for Turbulence Research - Annual Research Briefs*, pages 97–103, 2016.

[38] H. J. Bae, A. Lozano-Durán, S. T. Bose, and P. Moin. Turbulence intensities in large-eddy simulation of wall-bounded flows. *Phys. Rev. Fluids*, 3:014610, 2018.

[39] H. J. Bae, A. Lozano-Durán, S. T. Bose, and P. Moin. Dynamic slip wall model for large-eddy simulation. *J. Fluid Mech.*, 859:400–432, 2019.

[40] J. C. Del Alamo and J. Jiménez. Spectra of the very large anisotropic scales in turbulent channels. *Phys. Fluids*, 15(6):L41–L44, 2003.